JMEPEG (2012) 21:2263–2273
DOI: 10.1007/s11665-012-0196-1

1059-9495/$19.00

Gas Pressure Profile Prediction from Variable Strain Rate Deformation Paths in AA5083 Bulge Forming

F.S. Jarrar, L.G. Hector Jr., M.K. Khraisheh, and K. Deshpande

(Submitted September 8, 2011; in revised form January 30, 2012)

Two approaches to gas pressure profile prediction for bulge forming of AA5083 sheet under Quick Plastic Forming (QPF) conditions at 450 °C were investigated. The first was based on an algorithm internal to ABAQUS™ wherein the gas pressure results from maintaining a constant effective target strain rate at the dome pole. In the second, the nonlinear long wavelength stability analysis was combined with a single creep mechanism material model that accounts for hardening/softening. A series of stability curves, which denote combinations of strain and strain rate for unmitigated thinning and, ultimately, rupture of an AA5083 bar, were computed. These are based on a parameter that characterizes an assumed geometric non-uniformity, η. The associated uniaxial strains and strain rates were expressed in terms of von Mises effective strains and strains rates, and pressure profiles were computed. An ancillary approach to variable strain rate path prediction based on a thinning factor was used to suggest a suitable value of η in the stability analysis for a reasonable thinning level at the end of forming. Key advantages and disadvantages of both approaches to pressure profile prediction are examined relative to bulge forming time and thinning at a 50-mm dome displacement.

Keywords deformation stability, finite element simulation, quick plastic forming, superplastic forming

1. Introduction

In finite element (FE) simulations of high temperature gas pressure forming, the gas pressure is often linearly ramped to a constant value which is then held for all or part of the simulation. Additional ramping to higher pressures is required with complex die geometries. A little-explored alternative is the prediction of a pressure profile based on variable strain rate deformation computed from a stability criterion that determines conditions for thinning (or necking) instability in the sheet. Following this computed strain rate path (in theory) does not preclude local thinning of the sheet. Common practice in FE simulations is to adjust gas pressure profiles to maintain a constant strain rate at certain regions of the deforming sheet. For example, an algorithm is provided in the FE (implicit) ABAQUS™ code that adjusts the pressure profile to keep the strain rate within a certain pre-specified range.

Much of the existing literature on gas pressure profile prediction in high temperature sheet forming is focused either on uniaxial, biaxial, or plane strain deformation. For example, the work of Ren et al. (Ref 1), who experimentally determined an instability parameter as a function of strain for different strain rates in tensile tests of an Al-Li-Cu-Zr alloy under SPF conditions, is of notable interest. This parameter was previously extracted from Hart's tensile stability criterion (Ref 2, 3) by Caceres and Wilkinson (Ref 4) and Ash and Hamilton (Ref 5). When the instability parameter exceeded zero, an exponential increase in the neck growth rate was expected. Ren et al. (Ref 1) used this to determine the combinations of strain rate vs. critical strain (i.e., strain at which the instability parameter exceeded zero for a certain strain rate). Subsequent application resulted in the reduction of the uniaxial tensile testing time to failure from 35 to 13 min while maintaining the same elongation. Based on the stability criterion of Hart (Ref 2) and a Ti-6Al-4V constitutive model, Johnson et al. (Ref 6) generated a designed variable strain rate deformation path. The largest average strain rate corresponding to the instability criterion up to a strain of (∼1.5) in strain increments of (∼0.02) was computed. Uniaxial tensile tests were conducted to validate the analytically derived deformation paths. They concluded that such varying strain rate paths can result in significant deformation time savings.

While Ren et al. (Ref 1) and Johnson et al. (Ref 6) focused their investigations on uniaxial tensile tests, Ding et al. (Ref 7) computed a gas pressure profile to form sheet into a long rectangular box. The strain rate was controlled in the unsupported part of the sheet using an equation that fits a variable strain rate path based on Hart's 1D linear stability criterion (Ref 2) and a constitutive equation for Ti-6Al-4V. The simulation was conducted using the numerical model developed by Ghosh and Hamilton (Ref 8). Their results showed that the variable strain rate control in the free forming region was able to reduce the forming time by 13.4% with an increase of only 2.1% in the localized thinning compared with forming under a constant strain rate of 0.001 1/s. In 1997, Ding et al. (Ref 9) developed a linear stability

F.S. Jarrar, Mechanical Engineering Department, University of Kentucky, Lexington, KY; and Department of Mechanical Engineering, Faculty of Engineering and Technology, University of Jordan, Amman, Jordan; **L.G. Hector Jr.**, General Motors Company R&D Center, Warren, MI; **M.K. Khraisheh**, Masdar Institute of Science and Technology, Abu Dhabi, UAE; and **K. Deshpande**, General Motors Company, R&D, India Science Lab, Creator Building, ITPL, Bangalore 560066, India. Contact e-mails: f.jarrar@ju.edu.jo and firasjarrar2003@hotmail.com.z

criterion for biaxial stretching and used it to compute a variable strain rate path for Ti-6Al-4V. A commercial FE code was used to predict the pressure profile from the computed strain rate path in forming of a Ti-6Al-4V hemisphere at 900 °C. Yang et al. (Ref 10) used a step-change variable pressure which involves steps of isobaric forming with a non-constant strain rate within the superplastic region for bulge forming of Al 7475 alloy at 505 °C. They claimed to shorten the forming times compared with single-step constant pressure forming while achieving satisfactory thickness profiles.

In 1999, Khraisheh and Zbib (Ref 11) published a procedure for obtaining strain rate paths for gas pressure forming of superplastic Pb-Sn sheets based on biaxial tension tests. Constant strain rate bulge-forming experiments were conducted, and the actual time to failure for each strain rate (experiment) was recorded. The pressure profile was generated by following the pressure profile for the fastest strain rate up to 0.7 of the actual time to failure, then bumping down to the corresponding value of the pressure profile for the next fastest strain rate, and following it up to 0.7 of the actual time to failure, then bumping it down, and so on. Comley (Ref 12) used a maximum stress/strain failure boundary curve drawn on a series of experimentally obtained uniaxial tensile test constant strain rate curves to generate a variable strain rate path. His procedure was similar to that used by Khraisheh and Zbib (Ref 11); instead of using the latter's biaxial tension test data, he used the uniaxial tension data to generate a variable strain rate path for forming of a fine-grained Ti-6Al-4V pan.

Nazzal et al. (Ref 13), in 2004, derived a variable strain rate path based on the concept of Hart's stability criterion (Ref 2, 3) and a microstructure-based constitutive model for Ti-6Al-4V. The commercial FE code ABAQUS™ was used to simulate the forming of a deep rectangular box and an aircraft blowout door. The pressures required to form the parts using the variable strain rate paths were obtained and compared to those obtained by forming at two constant strain rates, one high and one low. Later, Thuramalla et al. (Ref 14) and Nazzal and Khraisheh (Ref 15) used the same procedure to compute a designed strain rate path for superplastic AA5083 alloy- and copper-based Coronze-638.

Nazzal and Khraisheh (Ref 16) proposed following the uniaxial nonlinear wavelength analysis of Hutchinson and Neale (Ref 17) as a basis for deriving the strain rate deformation paths in high-temperature sheet forming. This is a 1D analogue of the Marciniak and Kuczynski approach (Ref 18, 19). To test this approach, FE simulations of Mg AZ31 sheet forming into a deep rectangular box were conducted (Ref 16). Their numerical results showed that the designed strain rate path based on Hart's stability criterion was more conservative than that based on the nonlinear long wave analysis since, in the former, instability was predicted at lower strain levels. Nazzal and Khraisheh (Ref 16) modified the Hutchinson and Neale (Ref 17) analysis by means of a phenomenological constitutive relation that accounts for grain growth and cavitation. The resulting equation was then solved for a certain strain rate to yield a critical strain. Repeating the same for the whole range of strain rates and plotting the pairs of strain rates and the computed critical strains gave the strain rate deformation path.

In the present article, we extend the bulge forming model detailed in Jarrar et al. (Ref 20) to predict time-varying pressure profiles computed from the nonlinear long wavelength stability criterion for a 1D bar. Failure in the bulge-forming process usually occurs through unmitigated thinning at the dome pole followed by fracture along the rolling direction of the sheet. Results of FE simulations for AA5083 sheet formed under QPF conditions based on the GM R&D bulge tester are presented. The variable strain rate paths, from which are computed the pressure profiles, are derived from a set of solutions to a non-linear differential equation for the strain in that portion of the bar that is thinning. The solutions to the differential equation are displayed as a set of curves for selected values of an initial geometric non-uniformity η. These compare the ratio of the strain in the region of the bar that undergoes nonuniform thinning to that of the material undergoing uniform thinning. The associated uniaxial strains and strain rates are then expressed in terms of von Mises effective strains and strains rates and pressure profiles are computed for hemispherical bulge-forming AA5083 in QPF. An additional technique that leads to a single variable strain rate path based on a thinning factor is also presented for comparison with the nonlinear long wavelength analysis results. This approach involves no pre-assumed geometric inhomogeneity. The results of nonlinear long wavelength analysis and thinning factor approaches to pressure profile prediction are compared to those from the ABAQUS™ algorithm and the advantages and disadvantages of each are discussed in detail.

2. Material Constitutive Model

High-temperature (450 °C) AA5083 tensile data reported in Krajewski and Montgomery (Ref 21) was used to fit the single-term material model in Eq 1-3:

$$\dot{\bar{\varepsilon}} = \frac{K}{d^P}\left(\frac{\bar{\sigma}}{1-f_a}\right)^{1/n} \quad \text{(Eq 1)}$$

$$d = d(0) + c\bar{\varepsilon} \quad \text{(Eq 2)}$$

$$f_a = f_a(0)\exp(\psi\bar{\varepsilon}) \quad \text{(Eq 3)}$$

This model has been previously applied in FE simulations of superplastic-forming processes of both Al and Mg alloy sheets (Ref 13, 20, 22, 23). Note that $\bar{\varepsilon}$ and $\dot{\bar{\varepsilon}}$ denote the Von Mises effective strain and strain rate, respectively; $\bar{\sigma}$ is the Von Mises effective flow stress; n is a constant which is only equal to the strain rate sensitivity, m, at the start of deformation ($\bar{\varepsilon} = 0$); d is the average grain size; $d(0)$ is the initial grain size (~8.0 μm); $f_a(0)$ and f_a are the initial and current area fractions of voids, respectively; ψ is the void growth parameter; P and K are functions of the effective strain rate; and c is a material constant. To account for the change in microstructure during deformation, evolution equations for grain size d and area fractions of voids f_a are defined. The simple linear grain growth model in Eq 2 is similar to that used by Caceres and Wilkinson (Ref 24). The cavitation evolution model described by the exponential relation in Eq 3 is used, based on the assumption that cavitation is primarily controlled by the plastic flow of the surrounding matrix (Ref 25–27). While Eq 1 describes no specific creep mechanism, the two-term model in Taleff et al. (Ref 28) accounts for two independent creep mechanisms, viz., grain boundary sliding, and solute drag creep. However, the two-term model does not currently account for hardening/softening.

The AA5083 tensile data, which were measured at strain rates ranging from 0.0005 to 0.3 1/s, are shown in Fig. 1 as true stress (MPa) vs. true strain. A yield point effect (or local increase in the flow stress at small strains) appears at 0.01 1/s. At the largest effective strain rates of 0.1 and 0.3 1/s, the

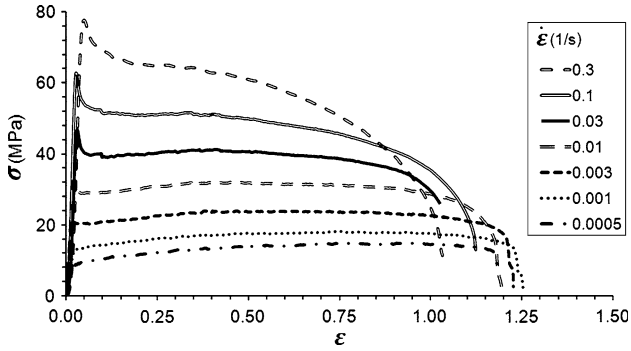

Fig. 1 True stress vs. true strain curves for the AA5083 alloy at 450 °C from tensile tests (Ref 21)

Table 1 Parameters resulting from the fit to Eq 1-3

Parameter	Value
n	0.5
P	$-3 - 0.43 \ln(\dot{\bar{\varepsilon}})$
$\ln(K)$	$-15.251 - 0.2021 \ln(\dot{\bar{\varepsilon}}) + 0.0346 \ln^2(\dot{\bar{\varepsilon}})$
$d(0)$ (μm)	8.0
c	2.5
$f_a(0)$ (%)	1.25
ψ	1.5

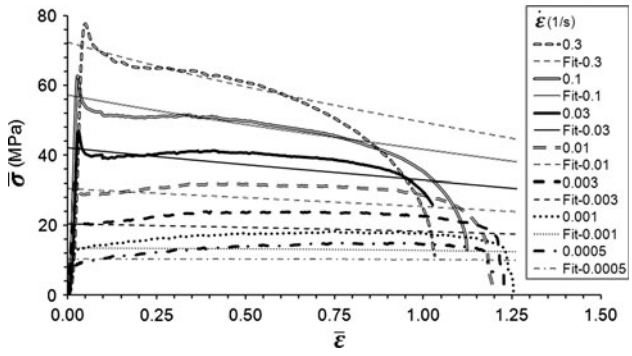

Fig. 2 Comparison of the material model, Eq 1-3, with fit parameters/functions in Table 1 (straight lines denoted with "-Fit" in the key) and the AA5083 450 °C tensile data (Ref 21)

material appears to soften beyond the yield point, although necking probably occurred not long after the yield point in the tensile tests.

By means of a fitting process detailed elsewhere (Ref 13, 22, 23), the parameters listed in Table 1 were computed for Eq 1-3. Note that the values of $d(0)$, c, $f_a(0)$, n and ψ were chosen based on the literature as no experimental data on the microstructural evolution in the material were available (Ref 29–32).

Figure 2 shows a plot of the single-term model in Eq 1-3 with the parameters in Table 3.1 against the experimental data in Fig. 1. The seemingly straight lines (each is actually a curve) represent the fit results in stress-strain space to the experimental data.

The strain rate sensitivity (m) is defined as

$$m = \frac{d(\log \bar{\sigma})}{d(\log \dot{\bar{\varepsilon}})} \qquad \text{(Eq 4)}$$

The material model in Eq 1-3 leads to the m vs. $\dot{\bar{\varepsilon}}$ variation as shown in Fig. 3. A high value of m denotes greater resistance to localized thinning. At a given strain rate, m decreases as deformation proceeds (i.e., as effective strain increases). In addition, a decrease in the effective strain rate $\dot{\bar{\varepsilon}}$ leads to a corresponding increase in m. Therefore, Fig. 3 suggests that as deformation proceeds, a decrease in the $\dot{\bar{\varepsilon}}$ to compensate for the decrease in m due to straining is preferable.

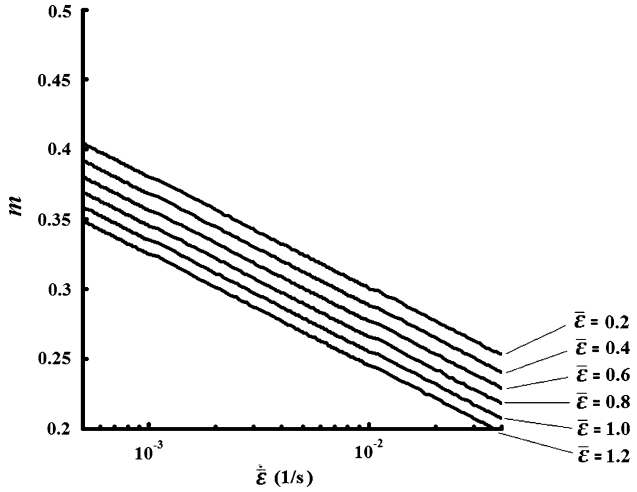

Fig. 3 Strain rate sensitivity (m) vs. effective strain rate for selected effective strains from the constitutive material model, Eq 1-3, for AA5083 at 450 °C

3. Finite Element Model

The FE model used in the present investigation is based on the bulge-forming instrumentation detailed in Bradley (Ref 33): this is shown in Fig. 4. The sheet is clamped along the die flange, as shown in Fig. 4(a, b), and forming occurs at 450 °C (neither the die nor the sheet is preheated in the simulations). The die has an inner diameter of 100-mm, a flange of 150-mm diameter, and a fillet radius of 5 mm. One-half of the die is shown in section view in Fig. 4(c). The circular AA5083 sheet, shown in Fig. 4(d), is of 114-mm diameter with an initial thickness of 1.2 mm. The sheet was meshed using 3D membrane elements [M3D4], whereas the die was meshed using 3D rigid elements. The final sheet mesh used in all simulations resulted from a series of careful mesh convergence tests. The sheet nodes located along the sheet circumference were fixed during the simulations to account for the restraint in the experiments. All simulations were conducted using the implicit solver in the commercial FE code ABAQUS™ 6.6.1 (Ref 34). The creep response was defined in a user-material subroutine containing the material model in Eq 1-3. Zero friction was assumed at the die entry radius.

4. Variable Strain Rate Deformation Path

4.1 Background

Forming at a constant strain rate that provides the highest m value produces the best obtainable forming quality or thickness distribution. However, this method requires long forming times. If the choice is made to sacrifice some of the quality to reduce

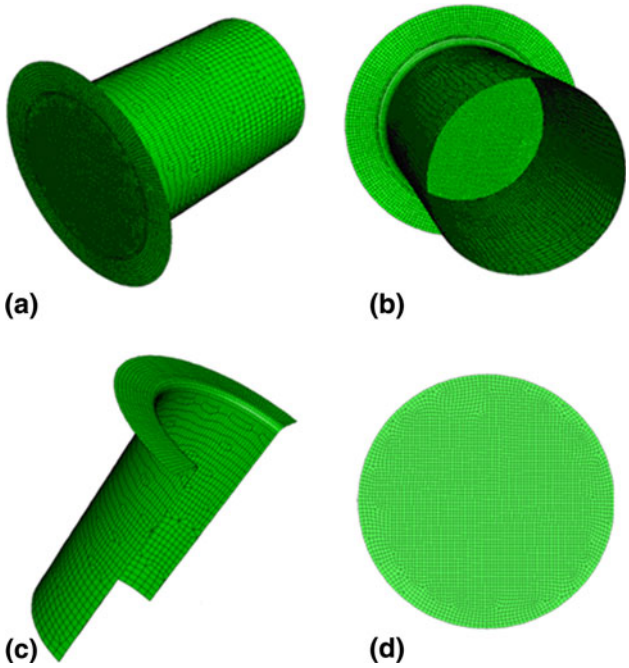

Fig. 4 (a, b) Different views of the die and sheet meshed together, (c) one half of the die mesh shown in section view, and (d) sheet mesh alone

the forming time, then there is no fundamental physical reason why hot gas pressure-forming processes must be conducted under constant strain rate. An alternative approach involves forming under a variable strain rate path such that unmitigated thinning and rupture are avoided. Here, we examine two theoretical approaches that result in variable strain rate deformation paths from which gas pressure profiles can be predicted. In the first, the nonlinear long wavelength stability analysis is applied (Ref 16, 17). The second approach is based on the thinning factor or the dome pole thickness divided by the average dome thickness measured along a cross-sectional contour cutting the dome into two equal halves through the pole. The latter results in a single relationship between effective strain rate, $\bar{\dot{\varepsilon}}$, and effective strain, $\bar{\varepsilon}$ (unlike the nonlinear long wavelength analysis approach that has as many such curves as η-values). The aim of both approaches is to compute a variable strain path that potentially leads to forming times that are less than those from constant strain rate forming, while maintaining as uniform a part thickness distribution as possible. .

4.2 Nonlinear Long Wavelength Stability Analysis

In this section, the tensile stability criterion due to Hutchinson and Neale (Ref 17) is used to generate a variable strain rate deformation path using the AA5083 material constitutive model, Eq 1-3. In their analysis (Ref 17), Hutchinson and Neale were motivated by the observation that a small amount of strain rate dependence can result in a large amount of straining before necking in bars. Consequently, they examined the deformation of a long cylindrical solid bar subjected to a time-dependent load, $F(t)$. The bar is assumed to contain a pre-existing geometric nonuniformity at which thinning localization and rupture can occur given the right conditions. The aim of the nonlinear long wavelength analysis is to find combinations of uniaxial strain and strain rate that will lead to rapid thinning and rupture of the bar for an assumed nonuniformity. Figure 5 shows a schematic of their model system.

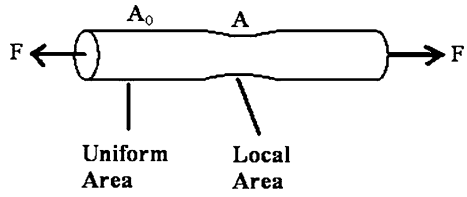

Fig. 5 Cylindrical bar under tension

Here, $A(t)$ is the current cross-sectional area of the "local" section (i.e., the section containing the inhomogeneity or deviation in the cross-sectional geometry of the bar). The current cross-sectional area of the uniform "perfect" section of the bar is denoted by $A_0(t)$. From this point on, the subscript 0 will refer to the uniform section of the bar as indicated in Fig. 5; any symbol without the subscript 0 refers to the local section of the bar following the nomenclature in Fig. 5. A constant uniaxial strain rate, $\dot{\varepsilon}_0$, is assumed in the uniform section of the bar. As deformation proceeds, the ratio $\varepsilon/\varepsilon_0$ (i.e., of the uniaxial strain in the local region to the uniaxial strain in the uniform region) is computed and closely monitored. If this ratio starts growing rapidly during deformation, then thinning increases rapidly in the local area ultimately leading to rupture (the details of rupture are not accounted for in the theoretical formulation or in any of the ensuing FE simulations).

Derivation of the variable strain rate path begins by rewriting the uniaxial version of Eq 1-3 for the uniform region of the bar in terms of the uniaxial stress, σ_0, as follows:

$$\sigma_0 = \bar{K}_0 d_0^{nP_0} \dot{\varepsilon}_0^n (1 - f_{a0}) \quad \text{(Eq 5)}$$

where

$$n = 0.5 \quad \text{(Eq 6)}$$

$$P_0 = -(3 + 0.43 \ln(\dot{\varepsilon}_0)) \quad \text{(Eq 7)}$$

$$\bar{K}_0 = \frac{1}{(K_0)^n} = \left[e^{\left\{ 0.0346(\ln(\dot{\varepsilon}_0))^2 - (15.251 + 0.2021 \ln(\dot{\varepsilon}_0)) \right\}} \right]^{-n} \quad \text{(Eq 8)}$$

$$d_0 = d(0) + c\varepsilon_0 = 8.0 + 2.5\varepsilon_0 \quad \text{(Eq 9)}$$

$$f_{a0} = f_a(0) e^{\psi \varepsilon_0} = 0.0125 e^{1.5\varepsilon_0} \quad \text{(Eq 10)}$$

The same relations also apply in the local region of the bar (with corresponding cross-sectional area A) in Fig. 5:

$$\sigma = \bar{K} d^{nP} \dot{\varepsilon}^n (1 - f_a) \quad \text{(Eq 11)}$$

where

$$n = 0.5 \quad \text{(Eq 12)}$$

$$P = -(3 + 0.43 \ln(\dot{\varepsilon})) \quad \text{(Eq 13)}$$

$$\bar{K} = \frac{1}{(K)^n} = \left[e^{\left\{ 0.0346(\ln(\dot{\varepsilon}))^2 - (15.251 + 0.2021 \ln(\dot{\varepsilon})) \right\}} \right]^{-n} \quad \text{(Eq 14)}$$

$$d = d(0) + c\varepsilon = 8.0 + 2.5\varepsilon \quad \text{(Eq 15)}$$

$$f_a = f_a(0) e^{\psi \varepsilon} = 0.0125 e^{1.5\varepsilon} \quad \text{(Eq 16)}$$

Note that the material constants $d(0)$, $f_a(0)$, ψ, c, and n have the same value in both regions (i.e., the uniform and local areas in Fig. 5).

The so-called long wavelength approximation is invoked in which the stress over each cross section is uniaxial and

uniform, with applied force F. This allows us to write the flow stresses in the local and uniform regions, σ and σ_0, respectively, as

$$\sigma = \frac{F}{A(1-f_a)} \quad \text{(Eq 17)}$$

$$\sigma_0 = \frac{F}{A_0(1-f_{a_0})} \quad \text{(Eq 18)}$$

Since F is the same throughout the entire bar, the following equilibrium equation applies:

$$F = A\sigma(1-f_a) = A_0\sigma_0(1-f_{a_0}) \quad \text{(Eq 19)}$$

Substituting for σ and σ_0 from the material constitutive models, Eq 5 and 11, into Eq 19 gives

$$A\bar{K}d^{nP}\dot{\varepsilon}^n(1-f_a)^2 = A_0\bar{K}_0 d_0^{nP_0}\dot{\varepsilon}_0^n(1-f_{a_0})^2 \quad \text{(Eq 20)}$$

Before proceeding further with the derivation, relations between the cross-sectional areas and the axial strains in the two sections of the bar are required. Assuming incompressibility, the uniaxial strains may be written as

$$\varepsilon = -\ln\left[\frac{A(1-f_a)}{A(0)(1-f_a(0))}\right] \quad \text{(Eq 21)}$$

$$\varepsilon_0 = -\ln\left[\frac{A_0(1-f_{a_0})}{A_0(0)(1-f_{a_0}(0))}\right] \quad \text{(Eq 22)}$$

where $A(0)$ and $A_0(0)$ are the cross-sectional areas at the start of plastic deformation in the local and uniform sections of the bar, respectively. Equation 21 and 22 may be written in terms of A and A_0 as follows:

$$A = \left[\frac{A(0)(1-f_a(0))}{(1-f_a)}\right]e^{-\varepsilon} \quad \text{(Eq 23)}$$

$$A_0 = \left[\frac{A_0(0)(1-f_{a_0}(0))}{(1-f_{a_0})}\right]e^{-\varepsilon_0} \quad \text{(Eq 24)}$$

Substituting for A and A_0 from Eq 23 and 24 into the equilibrium equation (20) gives

$$e^{-\varepsilon}\bar{K}d^{nP}\dot{\varepsilon}^n(1-f_a) = e^{-\varepsilon_0}\bar{K}_0 d_0^{nP_0}\dot{\varepsilon}_0^n(1-f_{a_0})\left[\frac{A_0(0)(1-f_{a_0}(0))}{A(0)(1-f_a(0))}\right] \quad \text{(Eq 25)}$$

The initial geometric nonuniformity, η, in the cross-sectional area of the bar in Fig. 5 is defined by

$$\eta = 1 - \frac{A(0)}{A_0(0)} \quad \text{(Eq 26)}$$

Use of Eq 26 in the analysis is a significant point of departure from the Hart (Ref 2) tensile stability analysis since it introduces nonlinearity into the stability analysis. Hence, an initially imperfect bar is associated with $\eta > 0$ where $A(0) < A_0(0)$. Noting that $f_a(0)$ is assumed to have the same value in both uniform and local regions, then using Eq 26, the equilibrium equation (25) maybe re-written as

$$e^{-\varepsilon}\bar{K}d^{nP}\dot{\varepsilon}^n(1-f_a) = e^{-\varepsilon_0}\bar{K}_0 d_0^{nP_0}\dot{\varepsilon}_0^n(1-f_{a_0})\frac{1}{(1-\eta)} \quad \text{(Eq 27)}$$

Raising both sides of Eq 27 to the power $1/n$ and substituting for the numerical values of n, the grain growth parameters d, d_0, area fraction of cavities parameters f_a, f_{a_0}, and the material state variables $\bar{K}$, $\bar{K}_0$, P, P_0, from Eq 5 to 16, gives the following nonlinear differential equation:

$$\dot{\varepsilon}e^{-2\varepsilon}\left[\frac{[8.0+2.5\varepsilon]^{-\{3+0.43\ln(\dot{\varepsilon})\}}}{e^{\{0.0346(\ln(\dot{\varepsilon}))^2-0.2021\ln(\dot{\varepsilon})-15.251\}}}\right]\left[1-\left(0.0125e^{1.5\varepsilon}\right)\right]^2 = \dot{\varepsilon}_0 e^{-2\varepsilon_0}\left[\frac{[8.0+2.5\varepsilon_0]^{-\{3+0.43\ln(\dot{\varepsilon}_0)\}}}{e^{\{0.0346(\ln(\dot{\varepsilon}_0))^2-0.2021\ln(\dot{\varepsilon}_0)-15.251\}}}\right] \times \left[\frac{(1-(0.0125e^{1.5\varepsilon_0})}{(1-\eta)}\right]^2$$

Recall that a constant strain rate $\dot{\varepsilon}_0$ is imposed in the uniform region (see Fig. 5). Thus, the only unknown in Eq 28 (assuming a value for η is supplied a priori) is the strain in the local region, $\varepsilon = \varepsilon(t)$. Equation 28 is a nonlinear, nonseparable ordinary differential equation of the form:

$$\dot{\varepsilon} = f(\dot{\varepsilon}, \varepsilon, t) \quad \text{(Eq 29)}$$

subject to the initial conditions:

$$\varepsilon(0) = 0 \quad \text{(Eq 30)}$$

$$\dot{\varepsilon}(0) = 1 \times 10^{-7}\ 1/\text{s} \quad \text{(Eq 31)}$$

The initial condition for the local strain rate, $\dot{\varepsilon}$, was set to the small number in Eq 31 instead of zero due to terms with $\ln(\dot{\varepsilon})$ in Eq 28.

Equation 28 was solved using the FE method-based commercial software, Comsol Multiphysics™ (Ref 35). While the methodology contained therein is mainly used for solving partial differential equations, the solution procedure for Eq 28 involved eliminating the spatial variation of the dependent variables, which is obtained by specifying only one element in the spatial computational domain. Neumann boundary conditions and the direct linear system solver "UMFPACK" were used. This solver is used for solving nonsymmetric sparse linear systems, $Ax = b$, using the nonsymmetric, multi-frontal method (Ref 36). The computations were performed for assumed values of η. For each η, different prescribed constant strain rates, $\dot{\varepsilon}_0$, in the uniform area of the bar were considered.

We consider the case of $\eta = 0.025$ in detail as an example. Figure 6 shows a plot of the ratio of the strain in the local area to the strain in the uniform area, $\varepsilon/\varepsilon_0$, against the strain in the uniform area, ε_0, for different prescribed strain rates, $\dot{\varepsilon}_0$ (see the figure key), in the uniform area of the bar. For each $\dot{\varepsilon}_0$, $\varepsilon/\varepsilon_0$ increases with increasing ε_0. The rate of this increase is nonlinear as observed in the various curves of Fig. 6. Each curve extends asymptotically to infinity at large ε_0; this corresponds to a theoretical designation for unmitigated thinning of the local area of the bar in Fig. 5 followed by rupture. There is a critical strain in the uniform area, $\varepsilon_{0\_\text{critical}}$, at which $\varepsilon/\varepsilon_0$ is sufficiently large as to signal the point of instability onset. We consider this to be the maximum obtainable strain in the uniform area. In this analysis, $\varepsilon_{0\_\text{critical}}$ was chosen to correspond to a slope of 0.2 for all curves. Although larger values could in fact be selected, the 0.2 value represented a reasonable compromise in that it is far enough away from the point where each curve adopts an infinite slope (smaller, but more conservative values could also be chosen). An increase of $\dot{\varepsilon}_0$ leads to a corresponding decrease of $\varepsilon_{0\_\text{critical}}$. Note that additional sets of curves similar to those in Fig. 6 were computed for η = 0.05, 0.01, 0.0075, 0.005, 0.0025, and

0.001. Behavior similar to that in Fig. 6 was observed in each case.

Figure 7(a) shows the "onset of instability" curves for all values of η investigated, while Fig. 7(b) is a magnified view of the curves corresponding to η = 0.025, and 0.05. At this point, the following generalization is made: the uniaxial strains and strain rates may be substituted by the von Mises effective strains and strain rates. Hence, ε_0 is replaced by the effective strain $\bar{\varepsilon}$ and $\dot{\varepsilon}_0$ is replaced with effective strain rate $\dot{\bar{\varepsilon}}$ in Fig. 7(a) (and the distinction between uniform and local areas as denoted in Fig. 5 is no longer relevant). Points on each curve, which are denoted by various symbols (see the key in Fig. 7a) correspond to combinations of $\dot{\bar{\varepsilon}}$ and $\bar{\varepsilon}$ that represent the limit of stable deformation at the fastest possible rate of deformation according to the nonlinear long wavelength analysis. Each point in the η = 0.025 curve was taken directly from Fig. 6 in the following manner. For example, $\bar{\varepsilon} = \varepsilon_{0\_critical} = 0.0263$ corresponds to $\dot{\varepsilon}_0 = 0.01 s^{-1}$ (labeled "A" in Fig. 7b). This is two-orders-of-magnitude smaller than $\bar{\varepsilon} = \varepsilon_{0\_critical} = 0.2718$ which corresponds to $\dot{\varepsilon}_0 = 0.001 s^{-1}$ (labeled "B" in Fig. 7b). Figure 7(a) results after additional pairs are added from curves similar to those in Fig. 6 but for the remaining values of η. The points are connected as a guide to the trends that are suggested in the data. Each curve in Fig. 7(a) divides the stability space into two regions. Points to the left of and below any given curve fall in the region of stable deformation for the corresponding value of η. Those points to the right of, and above each curve, fall in the region of unstable deformation for the corresponding η-value. Consider the η = 0.025 curve in Fig. 7(b). In the context of forming a metal hemisphere from a thin sheet, this curve suggests that small $\bar{\varepsilon}$ at the outset of forming require large $\dot{\bar{\varepsilon}}$-values. As the dome develops curvature and begins to adopt a hemispherical shape with increasing $\bar{\varepsilon}$, corresponding values of $\dot{\bar{\varepsilon}}$ decrease according to the η = 0.025 curve. We note that any one of the curves in Fig. 7(a) is a potential candidate for the variable strain rate deformation path for thin sheet deformation in a non-uniaxial stress state (for biaxial or plane strain deformation). However, the curve corresponding to η = 0.05 suggests that instability sets in just after straining begins.

In biaxial bulge forming, the strain rate is highest at the dome pole, and it stands to reason that a variable strain rate path should be computed based on the need to control deformation of the dome pole during forming. We note that the nonlinear long wavelength analysis has one significant drawback: choice of an appropriate value of η cannot be readily determined in high-temperature biaxial bulge experiments (for example).

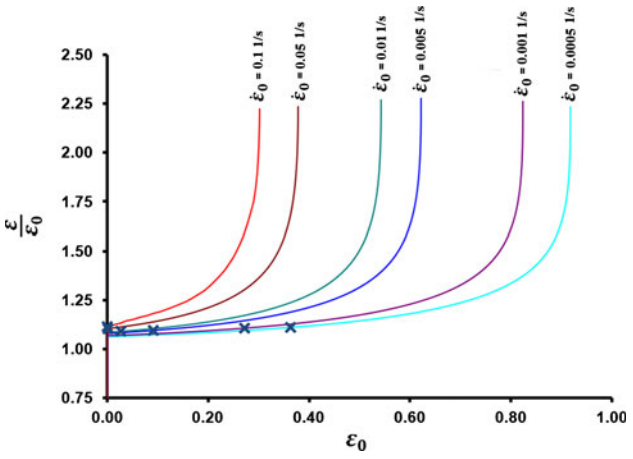

Fig. 6 Solutions to Eq 28 assuming η = 0.025 for selected $\dot{\varepsilon}_0$ in the uniform area (see Fig. 5). Note that ε_0 is the strain in the uniform area, and $\varepsilon/\varepsilon_0$ is the ratio of strain in local area to the strain in uniform area. The "×" symbols denote the points at which the slopes of the associated curves reach a value of 0.2

4.3 Variable Strain Rate Path from Thinning Factor Analysis

In Jarrar et al. (Ref 20), two sets of boundary conditions for gas pressure were applied in FE simulations of AA5083 high-temperature hemispherical bulge forming under QPF conditions. In the first set, the gas pressure followed a linear ramp to a constant value that was maintained for the duration of the simulation. In the second set of FE simulations, the gas pressure profile was computed (rather than prescribed at the outset of the

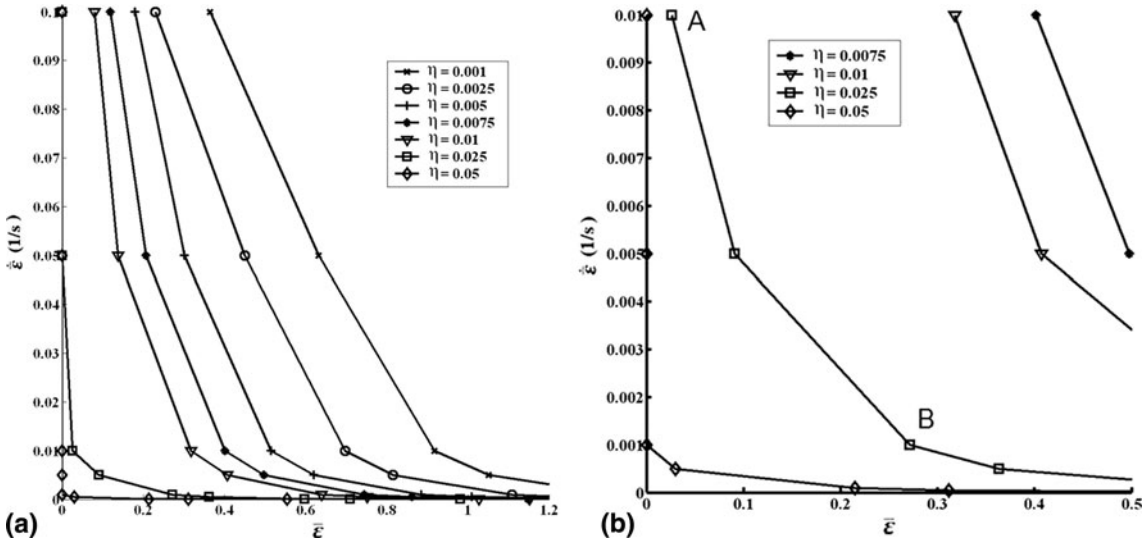

Fig. 7 (a) Onset of instability curves, obtained using the nonlinear long wavelength analysis criterion (Ref 17) for AA5083 at 450 °C, for different (selected) values of η. (b) Magnified view of the curves corresponding to η = 0.025, 0.05

simulation) using an algorithm internal to ABAQUS™ 6.6.1 (Ref 37). This algorithm attempts to maintain a constant strain rate at the dome pole during forming based on a user-chosen target effective strain rate. However, some fluctuations about the target strain rate are inevitable since the algorithm adjusts the pressure based on a set of specified ranges for the ratio of the maximum equivalent strain rate in the sheet at the current time step to the target effective strain rate. The pole height, thickness, and strain rate evolution profiles were computed for both sets of boundary conditions.

Jarrar et al. (Ref 20) also defined a thinning factor, β, as the dome pole thickness divided by the average dome thickness measured along a cross sectional contour cutting the dome into two equal halves through the pole. A perfect uniform thickness distribution corresponds to $\beta = 1$. The lower the thinning factor, the greater is the deviation in thickness distribution along the bulge profile. Hence, β was used as a quantitative measure of the uniformity of the dome thickness distribution at the end of the QPF FE simulation (i.e., when the sheet was formed into a hemispherical dome). Figure 8(a) shows the thinning factor β as a function of pole height, h, for six FE bulge simulation runs, each with a different constant effective target strain rate, $\dot{\bar{\varepsilon}}$, specified at the dome pole. Thirteen $\dot{\bar{\varepsilon}}$ values were considered in this study, with the highest being 0.04 1/s; however, to maintain clarity, only six curves are shown in Fig. 8(a) with corresponding $\dot{\bar{\varepsilon}}$ values listed in the key. Pole height was chosen as the abscissa value since the computed curves would not line up if in fact time were used; this would render the ensuing analysis much more challenging. The ABAQUS™ pressure control algorithm detailed in Jarrar et al. (Ref 20) was used to generate all of the curves. For a certain pole height, the smaller the value of $\dot{\bar{\varepsilon}}$, the larger is the value of β suggesting greater thickness uniformity. Notice, however, that the slope of each curve rapidly decreases as the dome height increases. The curves begin to significantly deviate from one another beyond a 20-mm pole height. The corresponding rapid decrease in β is an indication of a rapid increase in localized thinning. Figure 8(b) shows the effective strain, $\bar{\varepsilon}$, at the dome pole as a function of pole height, h, computed with the ABAQUS™ pressure control algorithm. Here, the curves begin to deviate from one another for $\bar{\varepsilon} \sim 0.4$. This agrees with a key observation made in Jarrar et al. (Ref 20) in that the U-shaped $\dot{\bar{\varepsilon}}$ evolution curves predicted for different constant pressure-forming profiles all achieving a minimum value for $\bar{\varepsilon} \sim 0.4$. The rapid increase in $\dot{\bar{\varepsilon}}$ that followed those minima is due to increased localized thinning at the pole.

Calculation of a variable strain rate path based on the variations of β with h in Fig. 8(a) first involves the selection of a series of ($\dot{\bar{\varepsilon}}$, $\bar{\varepsilon}$) pairs determined by a relative thinning factor, $\Delta\beta$; this factor is relative to a reference strain rate that leads to an "acceptable" forming result and another value of $\dot{\bar{\varepsilon}}$. We choose $\Delta\beta$ to be approximately two orders-of-magnitude smaller than β. As an example, we take $\dot{\bar{\varepsilon}} = 0.001$ 1/s as our reference strain rate since Jarrar et al. (Ref 20) demonstrated that this produces an AA5083 hemispherical dome in 1,074 s with $\beta = 0.62$ using the ABAQUS™ pressure control algorithm. We also assume that rupture will not occur at the end of forming (i.e., a 50-mm dome displacement) at $\dot{\bar{\varepsilon}} = 0.001$ 1/s. The first point of the variable effective strain rate path corresponds to that value of h on the highest strain rate curve (i.e., 0.03 1/s) at which the $\Delta\beta$ between the 0.03 and 0.001 1/s curves equals a user-chosen value. In the present case, we choose $\Delta\beta = 0.005$ (for reasons given below). The second point in the variable strain rate profile occurs on the 0.01 1/s curve in Fig. 8(a) when $\Delta\beta = 0.005$ 1/s relative to the 0.001 1/s curve. The process is continued in this fashion for all $\dot{\bar{\varepsilon}}$ in Fig. 8(a) above the reference strain rate of 0.001 1/s. The outcome of this procedure is a set of ($\dot{\bar{\varepsilon}}, h$) pairs for each $\dot{\bar{\varepsilon}}$ above 0.001 1/s. Finally, the chosen $\dot{\bar{\varepsilon}}$ values are plotted against the $\bar{\varepsilon}$ corresponding to the h-values in each pair following Fig. 8(b). Note that the resulting variable effective strain rate path would finally merge with the 0.001 1/s effective strain rate profile. Hence, imposition of $\Delta\beta$ allows one to "manually" determine a variable strain rate path so as to avoid excessive thinning of the dome pole, or, alternatively, to keep β within an acceptable small range during bulge forming.

Some comments on our choice of $\Delta\beta = 0.005$ 1/s are warranted. While this choice is largely at the discretion of the user, it is subject to some important considerations. The smaller the value of $\Delta\beta$, the more curves that are required in Fig. 8(a, b). This means that one would need more constant strain rate FE simulation runs using the ABAQUS™ pressure control algorithm. Assuming that there are cases where this additional effort may be warranted, a smaller value of $\Delta\beta$ would in fact result in more data points in the computed variable strain rate path.

The variable effective strain rate path generated by the thinning factor analysis for the AA5083 bulge forming at

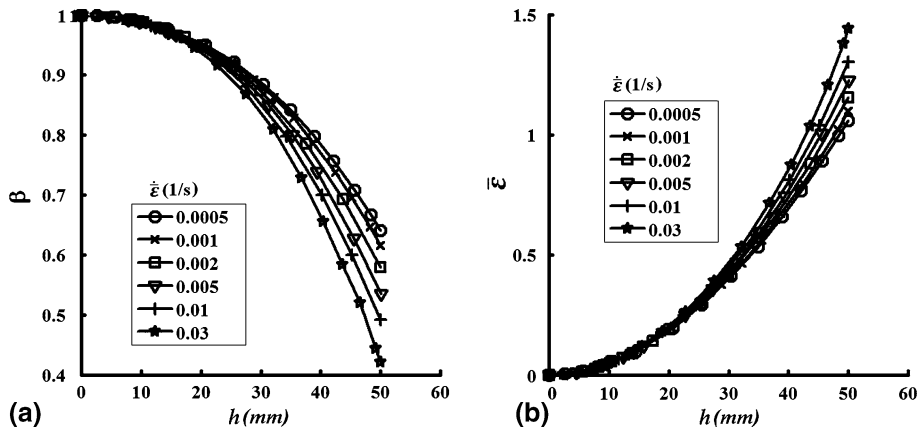

Fig. 8 Constant effective strain rate FE simulation runs results: (a) thinning factor vs. pole height (mm), and (b) effective strain at pole vs. pole height

450 °C is shown in Fig. 9. Also shown is the $\eta = 0.025$ curve from the nonlinear long wavelength analysis. Note that the curves were terminated at effective strain rates corresponding to $\dot{\bar{\varepsilon}} = 0.001$ 1/s. The most rapidly varying portion of the path sits below $\bar{\varepsilon} = 0.4$. The curve corresponding to $\eta = 0.025$ from the nonlinear long wavelength analysis is shown to be qualitatively similar.

5. Results and Discussion

Figure 10 compares the evolution of the thinning factor, β, with time (s) in AA5083 bulge-forming simulations which were terminated when the dome height reached 50 mm. Results from the three approaches to computing a variable strain rate path detailed above are compared. The blue symbols represent the FE-predicted β-values for selected constant (target) $\dot{\bar{\varepsilon}}$ values from the ABAQUS™ algorithm. These $\dot{\bar{\varepsilon}}$ values are listed in the key on the right side of the plot. Interestingly, the blue data points tend to follow a single nonlinear profile. The single red triangle denotes the result from the thinning factor analysis which is a single (β, *t*) pair. This is close to the $\dot{\bar{\varepsilon}} = 0.0012$ 1/s value from the ABAQUS™ algorithm. It is also close to the point corresponding to $\eta = 0.025$ from the nonlinear long wavelength analysis suggesting the proximity of their β-values. Notice that as is the case for the variable strain rate path generated by the thinning factor analysis, those generated by the nonlinear long wavelength analysis were all terminated at a cut-off strain rate value of 0.001 1/s. The green symbols from the nonlinear long wavelength analysis suggest that β increases with increasing η in a nearly linear fashion.

It is tempting to conclude from Fig. 10 that the nonlinear long wavelength analysis stands to offer little benefit over and above the ABAQUS™ and thinning factor analyses. However, it is important to consider key advantages and disadvantages associated with each approach to computing a variable effective strain rate path. Clearly, the positions of the blue symbols from the ABAQUS™ algorithm for constant strain rate forming suggest faster forming with comparable thinning (for the most part) relative to data from the nonlinear long wavelength analysis. In addition, the variable effective strain rate curve from the thinning factor analysis (see Fig. 9) required far less effort than that required of the nonlinear long wavelength analysis. However, unlike the nonlinear long wavelength analysis, there is no theoretical mechanism built-into the ABAQUS™ approach that attempts to avoid unmitigated thinning and rupture by varying the strain rate path followed during the course of forming. The thinning factor approach is clearly limited in that it provides only one variable effective strain rate curve, whereas there are an infinite number of possibilities with the nonlinear long wavelength analysis. Although it is not shown in Fig. 10, a green symbol for $\eta = 0.05$ would in fact sit above the blue "×" for $\dot{\bar{\varepsilon}} = 0.001$ 1/s in the constant strain rate formulation.

Clearly, the price that one must pay to avoid unmitigated thinning and rupture (in theory) by following the nonlinear long wavelength analysis is slower forming with thinning factors that are comparable to those from the ABAQUS™ approach. Since in the nonlinear long wavelength analysis, the $\dot{\bar{\varepsilon}} = 0.001$ 1/s, corresponding to the blue "×" in Fig. 10, was chosen as the reference or cut-off effective strain rate, our aim is to reduce the forming time while keeping a thinning distribution comparable to that associated with $\dot{\bar{\varepsilon}} = 0.001$ 1/s. Figure 10 shows that the upward pointing green triangle (nonlinear long wavelength analysis with $\eta = 0.025$), the upward pointing red triangle (thinning factor analysis), and the left pointing blue triangle (ABAQUS™ algorithm with a $\dot{\bar{\varepsilon}} = 0.0012$) are worth further investigation.

Figure 11 shows pressure profiles computed from the nonlinear long wavelength analysis and assuming a constant target effective strain rate. In all cases, the ABAQUS™ internal pressure control algorithm was used. The constant target strain

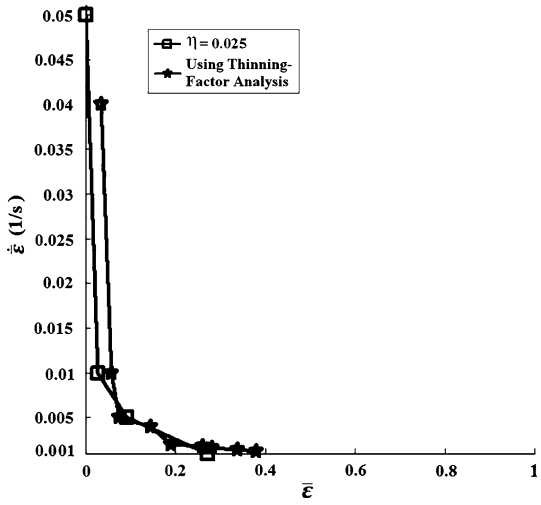

Fig. 9 Variable effective strain rate forming paths for bulge forming of AA5083 at 450 °C. The curve containing open squares was computed from the nonlinear long wavelength analysis with $\eta = 0.025$, and the curve containing the filled stars was computed from the thinning factor approach

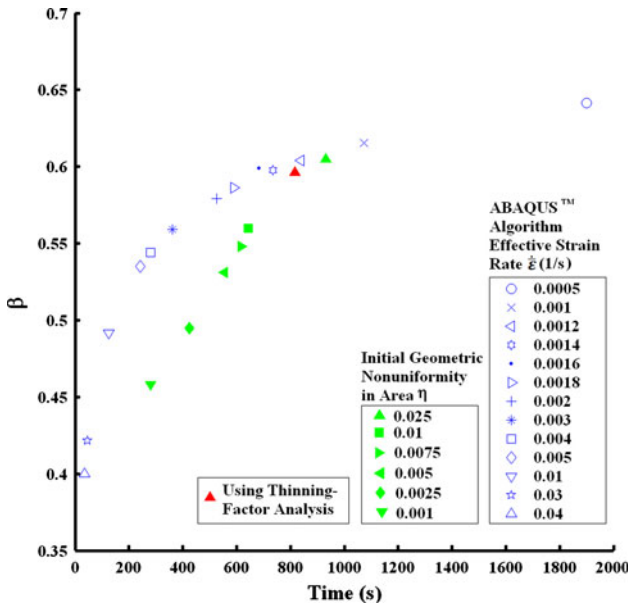

Fig. 10 Thinning factor, β, for the fully formed dome (i.e., when the pole height reached 50.0 mm) as a function of forming time (s) from the FE simulations assuming selected values at the dome pole and candidate-variable effective strain rate paths from the nonlinear long wavelength analysis. The red triangle corresponds to the (β, time) pair acquired from the thinning factor analysis in "Variable Strain Rate Path from Thinning Factor Analysis" section (Color figure online)

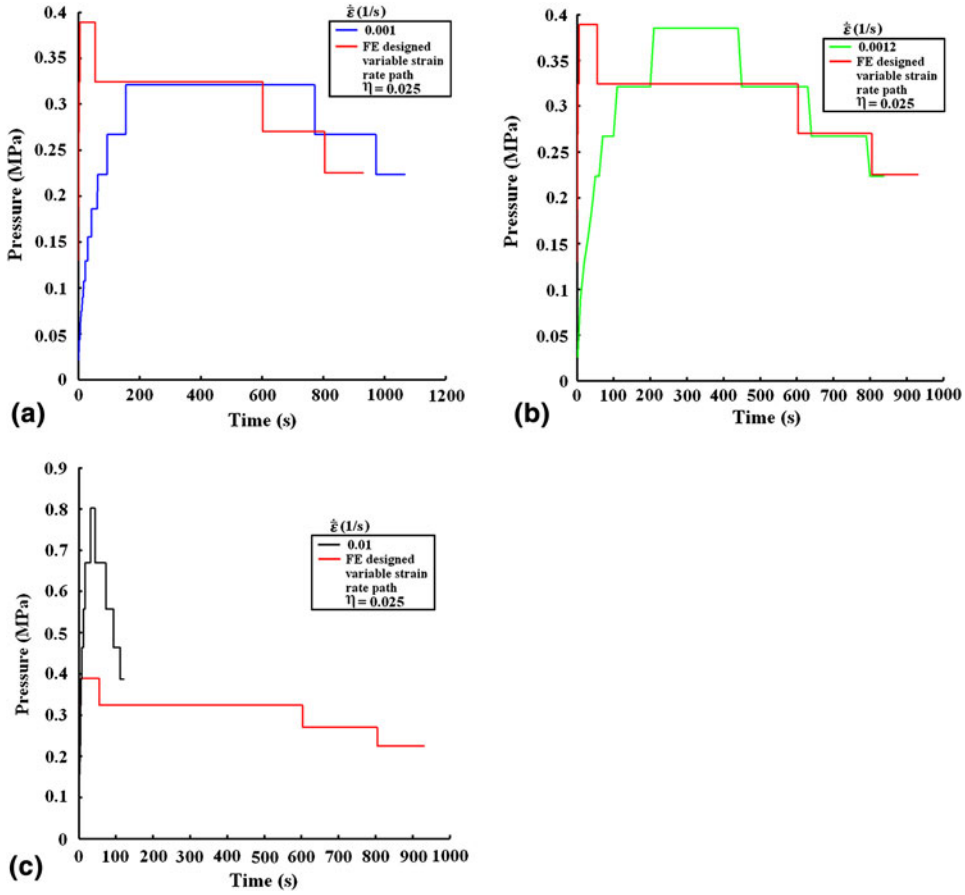

Fig. 11 Comparison between the computed gas pressure profiles for effective strain rates at the dome pole for: (a) 0.001 1/s (blue),(b) 0.0012 1/s (green), (c) 0.01 1/s (black), with that obtained using the designed variable effective strain rate path (η = 0.025) (red)

rates were substituted with the variable strain rate path from the nonlinear long wavelength analysis with η = 0.025. As mentioned above, additional $\dot{\bar{\varepsilon}}$ values were generated via interpolation between the data points in the curve in Fig. 9. We do not show results from the thinning factor analysis since these are comparable to those from the η = 0.025 value from the nonlinear long wavelength analysis. Three target strain rates are investigated, namely, 0.001 1/s (Fig. 11a), 0.0012 1/s (Fig. 11b), and 0.01 1/s (Fig. 11c). Under constant effective strain rate forming, the computed pressure follows a nearly linear ramp (with small "pauses" at specific pressures due to the step-wise nature of the ABAQUS™ pressure control algorithm), to a peak pressure value. This peak value persists for a period of time after which the pressure is decreased in a step-wise fashion. The pressure computed with the nonlinear long wavelength analysis instantaneously jumps to the peak value of 0.39 MPa which is held fixed for 60 s or so, after which point it decreases to a smaller value that is likewise held fixed for a protracted time period. The greatest differences in the shapes of the pressure profiles occur during the initial pressure-loading stage. Beyond this point, the pressure profiles from both approaches are qualitatively quite similar, although the associated pressure values can differ. The nonlinear long wavelength analysis tends to result in much more rapid ramping of the pressure than the constant target strain rate approach. We note that no experimental data are currently available from bulge simulations using the pressure profiles suggested in Fig. 11. This will require suitable gas pressure control hardware in experimental bulge forming tests.

Another issue that remains to be effectively explored is the extent to which material hardening/softening that is greater than that observed in AA5083 high-temperature tensile tests will contribute to the relationships between the different approaches, especially in the earliest stages of forming. Current efforts are focused on simulating bulge forming of Mg AZ31 with the different approaches to variable effective strain rate path prediction.

6. Conclusions

The major conclusions from this study are as follows:

1. The nonlinear long wavelength analysis and ABAQUS™ FE approaches predict gas pressure profiles that can be readily evaluated in experimental bulge forming to compare with existing profiles in which the pressure is linearly ramped to a constant value.
2. While both approaches have advantages and disadvantages, the nonlinear long wavelength analysis represents a theoretical framework in which unmitigated thinning and rupture can be avoided.
3. Comparing results from the variable strain rate path approach with η = 0.025 in the nonlinear wavelength

analysis, to that from forming with a constant effective strain rate of 0.001 1/s, shows that variable strain rate forming reduced the forming time by 13.2% with a decrease of only 1.67% in the minimum thickness at the pole.

4. Previous studies that considered such variable strain rate paths only compared results with one ''optimum'' strain rate path. This is in contrast to the present study. In order to completely evaluate the benefit of a predicted pressure profile, the forming time and thickness distribution must be compared with those resulting from forming under different strain rates, as depicted in Fig. 10 in this paper.
5. The pressure profile computed from the nonlinear long wavelength analysis involves an instantaneous ramp to a peak pressure, while that from ABAQUS™ is more gradual. At longer forming times, profiles from both approaches are qualitatively similar.
6. In the early stages of gas pressure forming of production parts, there is minimal contact with the die surface. Thus, a relatively high starting pressure, as predicted by the variable strain rate path approach here, provides a reasonable substitute for a linearly ramped starting pressure which is generated by the ''optimum'' constant strain rate forming approach.
7. The variable strain rate path generates a pressure profile that consists of relatively long isobaric forming steps. These are easier to apply in production-forming processes than the small pauses or steps required by the pressure profiles generated by the constant strain rate forming from ABAQUS™.
8. A main disadvantage of the nonlinear long wavelength analysis is that the value of the geometric nonuniformity in cross-sectional area, η, of the model bar on which the instability analysis is based, is not known a priori.
9. A reasonable choice for η that leads to the greatest value of β (the dome pole thickness divided by the average dome thickness measured along a cross-sectional contour cutting the dome into two equal halves through the pole) without rupture can be inferred from an ancillary analysis of β as function of dome pole height (requiring a separate set of FE calculations).
10. A main disadvantage of the ABAQUS™ constant strain rate approach to pressure profile prediction is the absence of any provision for avoiding unmitigated thinning and rupture.
11. A new numerical approach, the thinning factor control, was introduced in the present study. This method builds on FE simulation results, namely, the thinning factor evolution during deformation for different constant strain rates, to generate a designed variable effective strain rate path for fastest forming while maintaining an acceptable thickness distribution. The application of the procedure outlined in this work to other superplastic materials, with a higher m-value, is expected to provide even more favorable results.
12. While the stability analysis is based on a uniaxial criterion, the present approach to variable strain rate gas pressure forming can be readily extended to a two-dimensional criterion. Results from such a model can be compared to those of the present study to more thoroughly probe the advantages and disadvantages of the uniaxial criterion.

Acknowledgment

We would like to acknowledge the financial support of General Motors Company through a grant to the University of Kentucky.

References

1. B. Ren, H. Hamilton, and B. Ash, An Approach to Rapid SPF of an Al-Li-Cu-Zr Alloy, *5th International Aluminum-Lithium Conference*, E.A. Strarke and T.H. Sanders, Jr., Ed., (Williamsburg, VA), The Metallurgical Society, 1989
2. E.W. Hart, Theory of the Tensile Test, *Acta Metall.*, 1967, **15**, p 351–355
3. F.A. Nicholas, Plastic Instabilities and Uniaxial Tensile Ductilities, *Acta Metall.*, 1980, **28**, p 663–673
4. C.H. Caceres and D.S. Wilkinson, Large Strain Behavior of a Superplastic Copper Alloy I. Deformation, *Acta Metall.*, 1984, **32**(3), p 415–422
5. B.A. Ash and C.H. Hamilton, Strain and Strain-Rate Hardening Characteristics of a Superplastic Al-Li-Cu-Zr Alloy, *Scr. Metall.*, 1982, **22**, p 277–282
6. C.H. Johnson, C.H. Hamilton, H.M. Zbib, and S.K. Richter, Designing Optimized Deformation Paths for Superplastic Ti-6Al-4V, *Advances in Superplastic Forming*, N. Chandra, H. Garmestani, and R.E. Goforth, Ed., The Mineral, Metals & Materials Society, Warrendale, PA, 1993, p 3–15
7. X.D. Ding, H.M. Zbib, C.H. Hamilton, and A.E. Bayoumi, On the Optimization of Superplastic Blow-Forming Processes, *J. Mater. Eng. Perform.*, 1995, **4**(4), p 474–485
8. A.K. Ghosh and C.H. Hamilton, Superplastic Forming of a Long Rectangular Box Section—Analysis and Experiment, Process Modeling; Fundamentals and Applications to Metals, *Proceedings of American Society for Metals, Process Modeling Sessions, Materials and Process*, 1980, p 303–331
9. X.D. Ding, H.M. Zbib, C.H. Hamilton, and A.E. Bayoumi, On the Stability of Biaxial Stretching with Application to the Optimization of Superplastic Blow-Forming, *J. Eng. Mater. Technol.*, 1997, **119**, p 26–31
10. C.F. Yang, L.H. Chiu, and S.C. Lee, Superplastic Forming of 7475 Al Alloy by Variable-Pressure Blowing, *Scr. Mater.*, 1996, **34**(10), p 1555–1560
11. M.K. Khraisheh and H.M. Zbib, Optimum Forming Loading Paths for Pb-Sn Superplastic Sheet Materials, *J. Eng. Mater. Technol.*, 1999, **121**, p 341–345
12. P. Comley, Multi-Rate Superplastic Forming of Fine Grain Ti-6Al-4V Titanium Alloy, *J. Mater. Eng. Perform.*, 2007, **16**(2), p 150–154
13. M.N. Nazzal, M.K. Khraisheh, and B. Darras, Finite Element Modeling and Optimization of Superplastic Forming Using Variable Strain Rate Approach, *J. Mater. Eng. Perform.*, 2004, **13**(6), p 691–699
14. N.V. Thuramalla, M.A. Nazzal, and M.K. Khraisheh, Variable Strain Rate Forming Technique to Optimize Superplastic Forming of AA5083 Using Multiscale Stability Analysis, *Int. J. Form. Process.*, 2005, **8**(1), p 1–21
15. M.A. Nazzal and M.K. Khraisheh, The Effects of Stress State and Cavitation on Deformation Stability During Superplastic Forming, *J. Mater. Eng. Perform.*, 2007, **16**(2), p 200–207
16. M.A. Nazzal and M.K. Khraisheh, On the Stability of Superplastic Deformation Using Nonlinear Wavelength Analysis, *Key Eng. Mater.*, 2007, **344**, p 47–53
17. J.W. Hutchinson and K.W. Neale, Influence of Strain-Rate Sensitivity on Necking Under Uniaxial Tension, *Acta Metall.*, 1977, **25**, p 839–846
18. Z. Marciniak, K. Kuczynski, and T. Pokora, Influence of the Plastic Properties of a Material on the Forming Limit Diagram for Sheet Metal in Tension, *Int. J. Mech. Sci.*, 1973, **15**, p 789–805
19. Z. Marciniak and K. Kuczynski, Limit Strains in the Processes of Stretch-Forming Sheet-Metal, *Int. J. Mech. Sci.*, 1967, **9**, p 609–620
20. F.S. Jarrar, F.K. Abu-Fahra, L.G. Hector, Jr., and M.K. Khraisheh, Simulation of High Temperature AA5083 Bulge Forming with Hardening/Softening Material Model, *J. Mater. Eng. Perform.*, 2008, **18**, p 863–870
21. P.E. Krajewski and G.P. Montgomery, Mechanical Behavior and Modeling of AA5083 at 450°C, *Advances in Superplasticity and*

Superplastic Forming, E.M. Taleff, P.A. Friedman, P.E. Krajewski, R.S. Mishra, and J.G. Schroth, Ed., (Charlotte, North Carolina, USA), The Minerals, Metals & Materials Society (TMS), 2004, p 341–350
22. M.K. Khraisheh and F.K. Abu-Farha, Microstructure-Based Modeling of Anisotropic Superplastic Deformation, *Trans. NAMRI/SME*, 2003, **31**, p 41–47
23. F.K. Abu-Farha and M.K. Khraisheh, Analysis of Superplastic Deformation of AZ31 Magnesium Alloy, *J. Adv. Eng. Mater.*, 2007, **9**(9), p 777–783
24. C.H. Caceres and D.S. Wilkinson, Large Strain Behavior of a Superplastic Copper Alloy. Deformation, *Acta Metall.*, 1984, **32**, p 415–422
25. M.J. Stowell, Cavity Growth and Failure in Superplastic Alloys, *Metal Sci.*, 1983, **17**, p 92–98
26. C.L. Chen and M.J. Tan, Cavity Growth and Filament Formation of Superplastically Deformed Al 7475 Alloy, *Mater. Sci. Eng. A*, 2001, **298**, p 235–244
27. Y. Chino and H. Iwasaki, Cavity Growth Rate in Superplastic 5083 Al and AZ31 Mg Alloys, *J. Mater. Res.*, 2004, **19**(11), p 3382–3388
28. E. Taleff, L.G. Hector, Jr., J.R. Bradley, R. Verma, and P.E. Krajewski, The Effect of Stress State on High Temperature Deformation of Fine-Grained AA5083 Sheet, *Acta Mater.*, 2009, **57**, p 2812–2822
29. F. Li, D.H. Bae, and A.K. Ghosh, Grain Elongation and Anisotropic Grain Growth During Superplastic Deformation in an Al-Mg-Mn-Cu Alloy, *Acta Mater.*, 1997, **45**(9), p 3887–3895
30. M.A. Khaleel, M.T. Smith, and A.L. Lund, Cavitation During Multiaxial Deformation of Superplastic Forming, *Mater. Sci. Forum*, 1997, **243–245**, p 155–160
31. E. Tanaka, S. Murakami, and H. Ishikawa, Constitutive Modeling of Superplasticity Taking Account of Grain and Cavity Growth, *Mater. Sci. Forum*, 1997, **233–234**, p 21–28
32. H. Iwasaki, T. Mori, T. Tagata, M. Masatu, and K. Higashi, Cavitation in Superplastic Al-Mg Alloy, *Mater. Sci. Forum*, 1997, **233–234**, p 81–88
33. J.R. Bradley, Bulge Testing of Superplastic AA5083 Aluminum Sheet, *Advances in Superplasticity and Superplastic Forming*, E.M. Taleff, P.A. Friedman, P.E. Krajewski, R.S. Mishra, and J.G. Schroth, Ed., (Charlotte, North Carolina, USA) the Minerals, Metals & Materials Society (TMS), 2004, p 109–118
34. ABAQUS™, www.simulia.com. Accessed Mar 2009
35. COMSOL MultiPhysics™, http://www.comsol.com. Accessed Mar 2009
36. COMSOL MultiPhysics™, Reference Guide, Version October 2007 Comsol 3.4, 2007, p 508
37. ABAQUS™, Analysis User's Manual, vol. 3, Version 6.5, 2004, p 11.2.4–11.2.10